Monthly Notices
of the
ROYAL ASTRONOMICAL SOCIETY

MNRAS **454,** 1387–1392 (2015) doi:10.1093/mnras/stv2230

Wavelength self-calibration and sky subtraction for Fabry–Pérot interferometers: applications to OSIRIS

T. Weinzirl,[1]★ A. Aragón-Salamanca,[1] S. P. Bamford,[1] B. Rodríguez del Pino,[1,2] M. E. Gray[1] and A. L. Chies-Santos[3,4]

[1]*School of Physics and Astronomy, The University of Nottingham, University Park, Nottingham NG7 2RD, UK*
[2]*Centro de Astrobiología, INTA-CSIC, Villafranca del Castillo, E-28850 Madrid, Spain*
[3]*Departamento de Astronomia, Instituto de Fãsica, Universidade Federal do Rio Grande do Sul, Porto Alegre, R.S. 91501-970, Brazil*
[4]*Departamento de Astronomia, Instituto de Astronomia, Geofísica e Ciências Atmosféricas, Universidade de Saõ Paulo, 05508-900 São Paulo, SP, Brazil*

Accepted 2015 August 27. Received 2015 August 26; in original form 2015 July 14

ABSTRACT

We describe techniques concerning wavelength calibration and sky subtraction to maximize the scientific utility of data from tunable filter instruments. While we specifically address data from the Optical System for Imaging and low Resolution Integrated Spectroscopy instrument (OSIRIS) on the 10.4-m Gran Telescopio Canarias telescope, our discussion is generalizable to data from other tunable filter instruments. A key aspect of our methodology is a coordinate transformation to polar coordinates, which simplifies matters when the tunable filter data are circularly symmetric around the optical centre. First, we present a method for rectifying inaccuracies in the wavelength calibration using OH sky emission rings. Using this technique, we improve the absolute wavelength calibration from an accuracy of ∼5 to 1 Å, equivalent to ∼7 per cent of our instrumental resolution, for 95 per cent of our data. Then, we discuss a new way to estimate the background sky emission by median filtering in polar coordinates. This method suppresses contributions to the sky background from the outer envelopes of distant galaxies, maximizing the fluxes of sources measured in the corresponding sky-subtracted images. We demonstrate for data tuned to a central wavelength of 7615 Å that galaxy fluxes in the new sky-subtracted image are ∼37 per cent higher, versus a sky-subtracted image from existing methods for OSIRIS tunable filter data.

Key words: instrumentation: interferometers – techniques: imaging spectroscopy – galaxies: clusters: individual: Abell 901/902 – galaxies: distances and redshifts.

1 INTRODUCTION

A Fabry–Pérot interferometer, or etalon, is comprised of two reflecting plates working in a collimated beam. For a specific incidence angle of incoming light, the etalon transmits light of wavelength λ in a circular pattern of radius r around the optical centre. The range of wavelengths transmitted by the filter is adjusted by changing the separation between the reflecting plates.

Tunable filter (TF) instruments, often built with Fabry–Pérot interferometers, are proving to be a flexible and cost-effective implementation of spectrophotometry. The ability to precisely tune to an unlimited number of wavelengths in a specified interval circumvents the need to purchase arbitrary narrow-band filters (Bland-Hawthorn & Jones 1998). TF instruments are suitable for studies of emission and absorption lines in any redshift window, and they yield higher resolution ($R \sim 500$) than low-resolution grisms (González et al. 2014). However, the varying wavelength across the field of view makes data from TF instruments challenging to deal with. Background sky emission can be highly variable across an image in which bright OH sky emission lines appear as prominent rings (see Section 4 for an example). Full utilization of TF data requires a precise wavelength calibration and robust means of subtracting the complicated sky pattern.

In this Letter, we discuss refinements to the wavelength calibration and sky subtraction for TF data from the red mode on the Optical System for Imaging and low Resolution Integrated Spectroscopy instrument (OSIRIS; Cepa 2013; Cepa et al. 2013) on the 10.4-m Gran Telescopio Canarias (GTC) telescope. We specifically consider data of emission-line galaxies from the OSIRIS Mapping of Emission-line Galaxies in A901/2 (OMEGA) survey (Chies-Santos et al. 2015) in the Space Telescope A901/2 Galaxy Evolution Survey (STAGES) field (Gray et al. 2009). Our discussion is generalizable to similar TF instruments. We summarize the most important properties of the data in Section 2. Sections 3 and 4 address the wavelength calibration and sky subtraction, respectively.

★ E-mail: timothy.weinzirl@nottingham.ac.uk

© 2015 The Authors
Published by Oxford University Press on behalf of the Royal Astronomical Society

2 THE OMEGA SURVEY

Here, we briefly summarize the survey design and relevant data acquisition details of OMEGA. For the complete details, see Chies-Santos et al. (2015). OMEGA is based on a 90-h ESO/GTC Large Programme allocation (PI: A. Aragón-Salamanca). It was designed to yield deep, spatially resolved emission-line images and low-resolution spectra covering the H α and [N II] lines for galaxies in the STAGES supercluster.

An exposure time of 600 s was adopted to achieve an S/N $\geq$ 10 in the line flux for galaxies with $17 \leq R \leq 23.5$ (Vega) continuum magnitudes. Deblending the H α and [N II] lines required a TF full width at half-maximum (FWHM) bandwidth of 14 Å and a wavelength sampling of 7 Å. The 7615–7734 Å wavelength range was covered in 18 increments to probe the full cluster velocity range. 20 telescope pointings were used to map 0.18 deg^2 of the supercluster.

Observations were taken over three observing seasons between 2012 and 2014. Clear sky conditions were required, and the moonlight was grey or dark. Different exposures for a given field were not necessarily observed in the same night or under consistent environmental conditions (e.g. temperature, humidity, seeing). The median seeing was ~0.9 arcsec, and always $\leq$1.2 arcsec. Additional details concerning these observations and the data reduction are provided in Chies-Santos et al. (2015).

3 WAVELENGTH SELF-CALIBRATION

González et al. (2014) show that the radial dependence of wavelength for the OSIRIS red TF is given by the expression

$$\lambda = \lambda_0 - 5.04r^2 + a_3(\lambda)r^3, \quad (1)$$

where

$$a_3(\lambda) = 6.0396 - 1.5698 \times 10^{-3}\lambda + 1.0024 \times 10^{-7}\lambda^2, \quad (2)$$

λ_0 is the effective wavelength at the optical centre (i.e. the wavelength to which the TF instrument is tuned), r is measured in arcmin, and wavelengths are measured in Å. After applying the above calibration to our data, we still found significant wavelength offsets between the spectra of galaxies imaged independently in partially overlapping fields. The magnitude of the offsets varied from field to field, but it was in general enough to affect flux calibration and velocity measurements.

Assuming the radial dependence of wavelength in equation (1) is correct (which we will test later in this section), we attempt to update the λ_0 term based on the positions of sky rings in the images. Adjusting λ_0 in this way essentially corrects for instrument tuning inaccuracies.

The high-resolution ($R \approx 35\,000$ at 7000 Å) spectral atlas of Osterbrock et al. (1996) shows multiple OH emission lines populate the spectral range of our observations. We therefore simulate how the sky spectrum should look given our chosen TF bandwidth (14 Å). We convolve an OSIRIS sky spectrum of resolution higher than our data with a 14 Å FWHM Gaussian kernel. Fig. 1 shows the original sky spectrum and the result of the convolution; central wavelengths of the sky lines in the low-resolution spectrum are measured simply as the local maxima of the peaks. The relative strengths of the night sky emission lines are known to vary with time, and this will affect the adopted convolved wavelength of the blended lines, limiting the accuracy of the wavelength calibrations. To evaluate the variability of this effect, we also convolved an independent sky spectrum taken from Hanuschik (2003) taken with the European Southern Observatory's Ultraviolet and Visual Echelle Spectrograph (UVES). All sky lines obtained after convolving the UVES spectrum agree to within ±0.14 Å of those from the convolved OSIRIS sky spectrum.

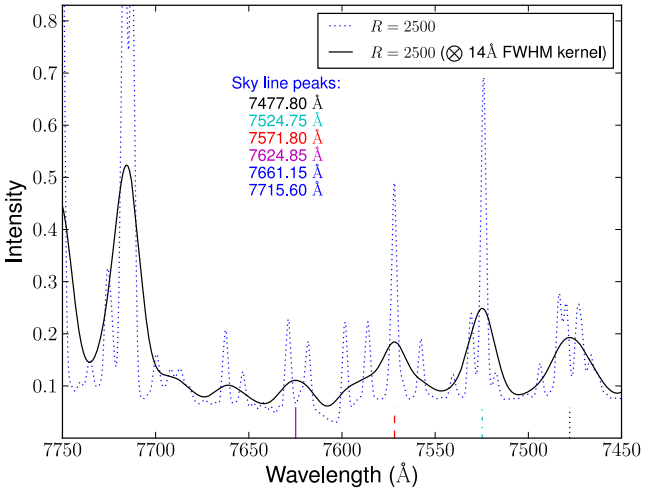

Figure 1. The dashed curve is an intermediate-resolution ($R = 2500$) sky spectrum from the GTC. The solid curve results after convolving the dashed curve with a Gaussian kernel having an FWHM equal to the resolution of our data (14 Å). The peaks of the sky lines in the convolved spectrum are measured as the local maximum around each peak. The colour coding and reversed wavelength scale make for easy comparison with Figs 2 and 3.

We generate sky spectra for every exposure to compare with the sky spectrum in Fig. 1 (see Chies-Santos et al. 2015 for the observing strategy). For the sky background, we simply use an intermediate-step frame from the OSIRIS Offline Pipeline Software (OOPS; Ederoclite 2012) that has been through all processing steps (overscan subtraction, bias subtraction, flat fielding) except sky subtraction. (Alternatively, one could also directly use the sky models discussed in Section 4.)

The sky images are converted from Cartesian $x - y$ coordinates to polar $r - \theta$ coordinates, where r is the distance of a pixel to the optical centre and θ is the angle from the image y-axis. The conversion of Cartesian to polar coordinates is made by backward mapping. A grid in polar coordinates with the desired resolution in $r - \theta$ is initialized, and then to each $r - \theta$ pixel the intensity at the corresponding Cartesian pixel is assigned. We have used a resolution of 1 pixel (0.25 arcsec) in r and 1° in θ. Note, we adopt the optical centre reported by OSIRIS handbook[1] of $X_0 = 772$, $Y_0 = 976$ (CCD1) and $X_0 = -35$, $Y_0 = 976$ (CCD2).

The example transformation in Fig. 2 shows the sky emission rings become vertical columns in the $r - \theta$ plane. We have checked that there is no systematic change in the column centres (i.e. tilt) with θ. This means the sky emission rings have circular symmetry and that we can accurately characterize their centre with a single measure after collapsing the $r - \theta$ plane in θ.

The two-dimensional images are collapsed into one-dimensional spectra by taking the median across all θ at a given r. The example in Fig. 3 shows a sky spectrum for an image where the central wavelength is approximately 7643 Å. Comparing Fig. 3 to Fig. 1, while noting the central wavelength of 7643 Å, implies the visible sky lines in the spectrum correspond to wavelengths 7624.85, 7571.80, 7524.75, and 7477.8 Å. The central wavelength of each

[1] http://www.gtc.iac.es/instruments/osiris

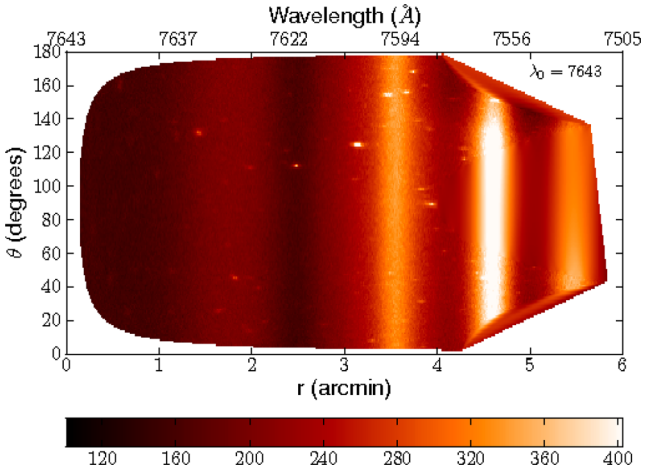

Figure 2. This image is a two-dimensional sky map after conversion to polar coordinates. The wavelength at the centre of the image is approximately 7643 Å, and the actual wavelength probed declines from the centre outwards. The vertical columns of relatively higher intensity correspond to sky emission rings. These columns show no systematic tilt and demonstrate the sky emission has circular symmetry.

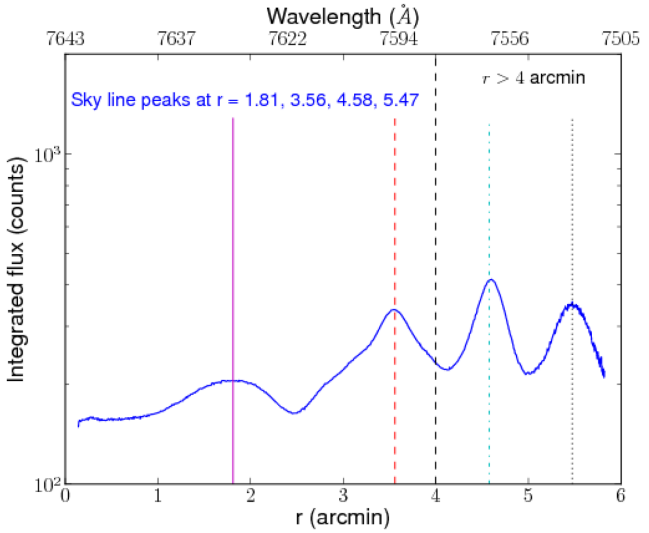

Figure 3. This one-dimensional spectrum is the result of median collapsing across θ the sky map in Fig. 2. The peaks correspond to sky lines at 7624.85, 7571.80, 7524.75, and 7477.8 Å. The latter two lines are beyond a radius of 4 arcmin and are not used in the recalibration.

sky line in a one-dimensional spectrum is measured simply as the local maximum emission.

Reliable observations in the OSIRIS red TF data are limited to a circular field of view of radius 4 arcmin (960 pixels); beyond 4 arcmin, there can be contamination by other orders. For all sky lines at radii less than 4 arcmin from the optical centre, we measure the expected wavelengths of the sky lines using equation (1). The average offsets between the actual and expected sky line wavelengths are the requisite adjustments to λ_0 for a single exposure. As a simplification, we calculate average adjustments to λ_0 as a function of tuning wavelength and field. The adjustments were typically ∼5 Å, but they were as high as ∼11 Å in some cases.

In Fig. 4(a), we test whether the updated calibration still follows the relation from González et al. (2014; our equation 1). We plot $\lambda_{\rm sky} - \lambda_0'$, where $\lambda_{\rm sky}$ is the sky line wavelength and λ_0' is the re-

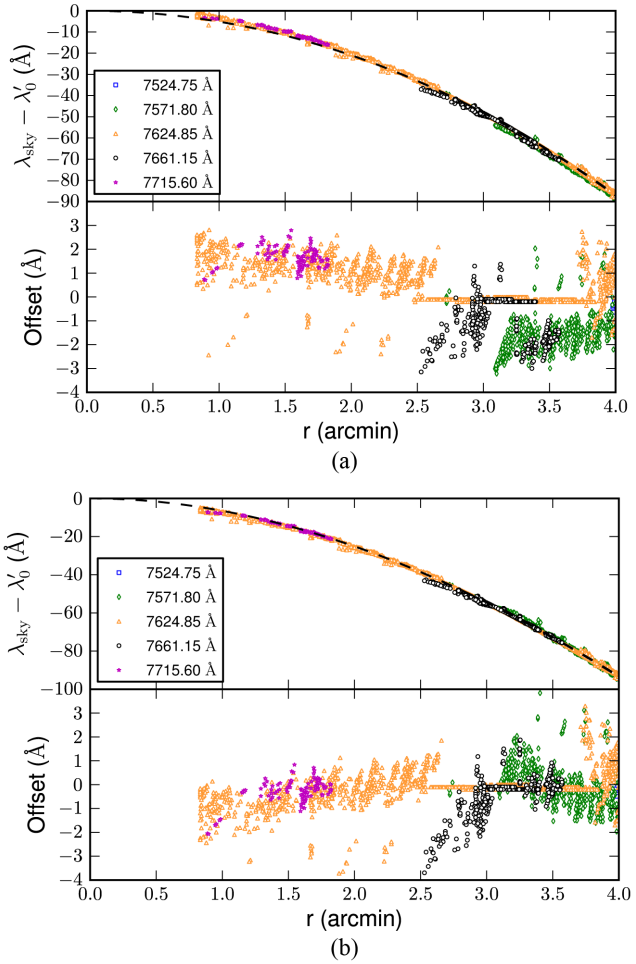

Figure 4. In panel (a, top), the difference in the sky line wavelength ($\lambda_{\rm sky}$) and the recalibrated tuning wavelength (λ_0') is plotted against radius from the optical centre. The dashed line is the wavelength calibration derived by González et al. (2014). The bottom panel shows the corresponding residuals. The bands of near zero residual are from exposures with only one sky line at $r < 4$ arcmin. Panel (b) is similar but instead uses the result of the iterative refitting procedure discussed in Section 3.

calibrated tuning wavelength, for sky lines within 4 arcmin of the optical centre. The line is the relation from González et al. (2014). Offsets of ∼2–3 Å from the calibration are common. González et al. (2014) assumed the CS-100 Fabry–Pérot controller in OSIRIS is strictly linear in its gap spacing–control variable (Z) relation, and attributed all non-linearities to phase dispersion effects in the dielectric coatings of the etalons. The discrepancy we measure here may be an indication that the assumption of linearity is not strictly true.

While the relation from González et al. (2014) is accurate over a large wavelength range, systematic offsets up to 3 Å can occur in certain narrow wavelength ranges. One can proceed with this level of disagreement if it does not affect the accuracy of the science, e.g. H α-based star formation rates. For redshift determinations, however, a 2 Å error (93 km s^{-1}) is large.

We propose an iterative method to refit the wavelength calibration and reduce the typical error down to 1 Å. In our data set, most (89 per cent) exposures with more than one sky line inside 4 arcmin of the optical centre contain the sky line at 7624.85 Å. We focus on these exposures and perform an iterative procedure.

(i) Calculate offsets relative to the González et al. (2014) calibration for sky line 7624.85 Å as a function of tuning wavelength setting (λ_0) and field.

(ii) Apply these offsets to the remaining sky lines at wavelengths other than 7624.85 Å. To these sky lines, fit the same functional form justified by González et al. (2014), but with more free parameters for better agreement, namely

$$\lambda = \lambda_0 + a_2 r^2 + a_3(\lambda) r^3, \quad (3)$$

where

$$a_3(\lambda) = a_{3,0} - 1.5698 \times 10^{-3}\lambda + 1.0024 \times 10^{-7}\lambda^2. \quad (4)$$

The free parameters are a_2 and $a_{3,0}$, which are fixed to -5.04 and 6.0396 by González et al. (2014).

(iii) Iterate until the model converges with the sky lines at 7624.85 Å. In subsequent iterations, the offsets for the 7624.85 Å sky line are calculated relative to the newly fit model in the above step.

Fig. 4(b) shows the result after 10 iterations of this procedure. The fit is noticeably better overall (although residuals for a few measurements slightly worsen). Most (85.5 per cent) of the individual sky line measurements agree to within 1 Å of the new calibration. This is an improvement over Fig. 4(a) where that percentage is only 50.7 per cent for the González et al. (2014) solution.

Using the new calibration from Fig. 4(b), we calculated average corrections to λ_0 for each combination of wavelength setting and field in our data. Correcting the central wavelengths with the offsets calculated from the sky lines in this way yields a wavelength calibration accurate to within 0.5 Å for most (76 per cent) of the individual image frames, and accurate to within 1 Å for 95 per cent of the frames. The 1 Å level of accuracy is a success considering it is ∼7 per cent of the 14 Å instrumental resolution. The calculated corrections do not vary in any systematic way with date of observation, ambient temperature, or humidity. The mean offset does vary weakly with λ_0. The average offset declines from 2 Å at $\lambda_0 = 7620$ Å to -2.7 Å at $\lambda_0 = 7734$ Å.

It is important to point out that OSIRIS uses a non-standard phase-correction scheme that may affect the generalizability of this method to very different Fabry–Pérot interferometers. Additional pre-requisites for the application of this method are that the data be circularly symmetric around the optical centre and that wavelength dependence on detector position be radially symmetric. Our wavelength recalibration benefitted from having a common sky line across most exposures; not having this may produce poorer results. This technique's accuracy may further be limited by variation in sky line relative intensities, which can perturb the effective peak positions of the blended sky lines in the low-resolution OSIRIS sky spectra. For our TF bandpass (∼14 Å) and spectral range, the variability is small (±0.14 Å), but it may be worse in other instances.

4 SKY SUBTRACTION

In this section, we overview a new sky subtraction technique for TF data. The current sky subtraction in OOPS works by artificially dithering images on a three-by-three pixel grid (Ederoclite 2012). Median combining the dithered images produces an estimate of the sky background. Visual inspection of the sky maps, such as the one shown in Fig. 5(a) tuned to a central wavelength of 7615 Å, shows that the outer envelopes of galaxies remain in the sky background. Applying this sky background oversubtracts and eliminates the real outer envelopes of galaxies.

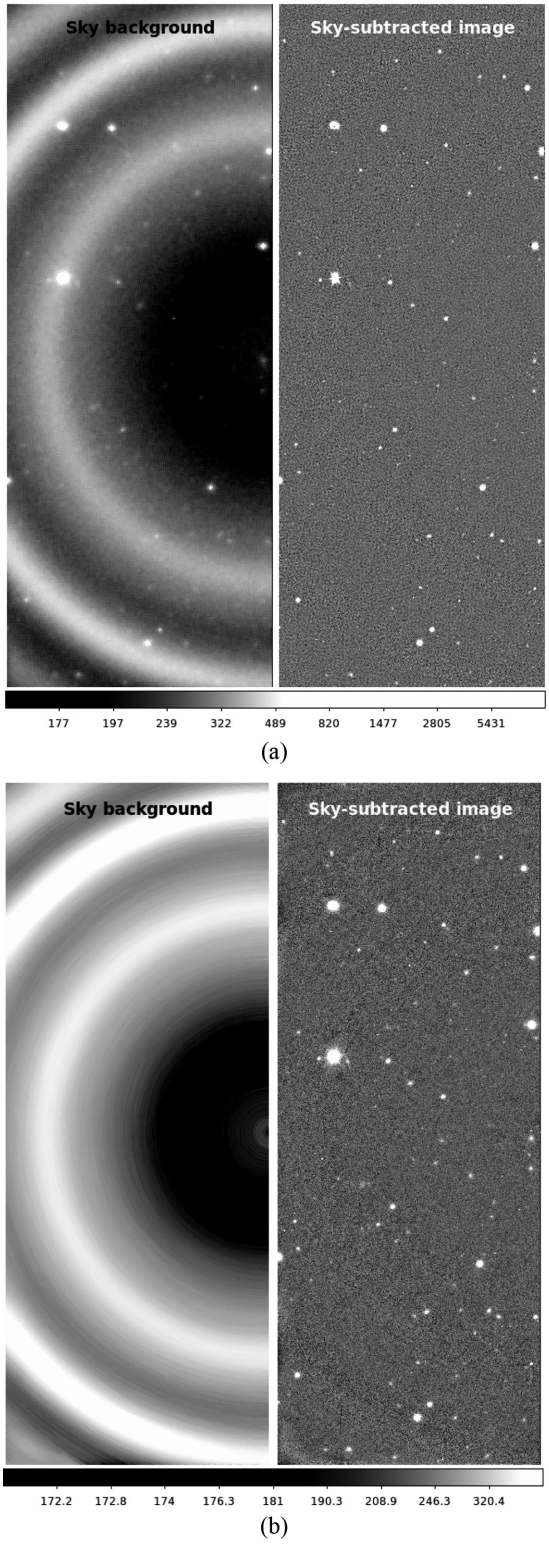

Figure 5. For a representative exposure, panel (a) shows the sky background measured by OOPS (left-hand), and the corresponding sky-subtracted image (right-hand). The wavelength at the optical centre is approximately 7615 Å. For the same exposure, panel (b) shows an example of the sky map generated by the filtering technique outlined in Section 4 (left-hand) and the corresponding sky-subtracted image (right-hand). Median filtering was performed with dr set to 3 pixels (0.75 arcsec), a total filter size drdθ of 170 pixel radians, and iterative 3σ clipping. The colour bars show the colour stretch and are similar in both panels.

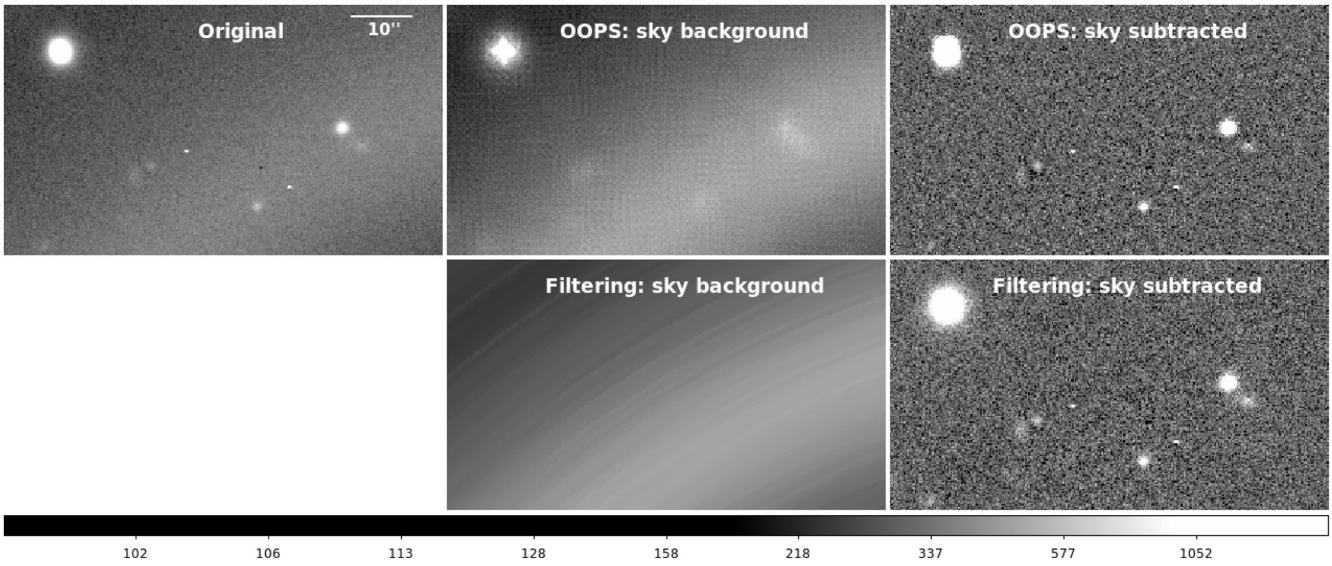

Figure 6. A magnified view of Figs 5(a) and (b) showing a subregion containing both bright extended sources and compact faint sources. The top row shows the original flat-fielded image still containing the sky, the sky background from OOPS, and the final OOPS sky subtraction. The second row shows the sky background inferred from filtering and the resulting sky-subtracted image. The colour bar shows the colour stretch and applies to all panels.

We have developed an alternate approach to sky subtraction that mitigates the problem of source oversubtraction. The basic idea is to remap the flat-fielded images from Cartesian to polar coordinates (Section 3) and then run a median filter, in polar coordinates, along circular arcs of grouped radii, to filter out sources and leave behind an estimate of the sky background.

Circular symmetry in the background sky emission means that the sky changes quickly in r but is relatively stable across θ at a given r (Fig. 2). However, sky subtraction is not as straightforward as converting a collapsed one-dimensional sky spectrum (e.g. Fig. 3) into a two-dimensional circularly symmetric sky model. Because in some cases, the sky varies as a slow function of θ (5–10 per cent amplitude) due to imperfect flat-fielding, this simplified approach is less effective at removing broadened sky line emission than the method we will adopt.

The simplest application of a median filter is to filter over θ at a given r with a fixed window size (as measured in polar image pixels). This is also not recommended. Sources at small distances from the optical centre are not effectively removed because, for a fixed window size in polar coordinates, the number of pixels from the original image that contribute to the median becomes very small at small radii. A significant improvement in filtering performance is achieved by fixing the median filter window to contain an approximately constant number of pixels from the original image. Thus, for a given filtering window drdθ, the number of polar image pixels in the filter varies inversely with radius, and this ensures a sufficient number of pixels from the original image are filtered over at small radii.

As we show below, changing the width of dθ has little effect on the outcome of the sky subtraction. Changing dr, however, has a more significant effect. Increasing dr incorporates more image pixels into the filter, improving robustness and increasing the speed of the filtering. Raising dr too high yields a sky map with too low spectral resolution that introduces artefacts in the sky-subtracted images. As a compromise, we have chosen to set dr to 3 pixels (0.75 arcsec, 0.57 Å at $r = 4$ arcmin), small enough to be beneficial but not problematic.

Because the dependence of λ on r is approximately quadratic, a more sophisticated approach would be to change dr according to quadratically varying bins such that each radial bin represents a constant $\Delta\lambda$ decrement in wavelength. We have tested this binning pattern with our data. Even if we make the radial bins 1-pixel wide at large radii, the radial bins near the optical centre become so wide that often include many sources which are not effectively removed by the median. This leaves behind residual background light in the sky-subtracted images that would bias the photometry of centrally located sources. Other, more complex, radial binning patterns could also be applied, but we did not find they yield any significant improvement over our method. Nevertheless, while this increased complexity is not necessary with our data, it may prove useful with different data sets.

As a further refinement, we apply σ clipping to prevent the extended haloes of bright sources from being smeared into the background sky, which causes local oversubtraction of the sky and leads to dark haloes around galaxies. We have found that iteratively clipping to 3σ for 5 iterations is sufficient to nullify this effect.

Fig. 5(b) shows the results of applying the filtering to the same exposure highlighted in Fig. 5(a). For this example, we have fixed dr to 3 pixels and the total filter size drdθ to 170 pixel radians, corresponding to a filter size of 20° at $r = 2$ arcmin. The sky background is much smoother than what is provided by the current algorithm in OOPS (Fig. 5a, left-hand panel), and the sky-subtracted sources in the right-hand panel of Fig. 5(b) are clearly brighter than in Fig. 5(a). Binning in r, however, yields sky models with band-like artefacts of width dr (see Fig. 6, row 2, column 2). The change in brightness between bands is typically ∼1–2 per cent of the sky background, smaller than the background shot noise (3–4 per cent).

Fig. 6 gives a magnified view of the sky subtraction in an image subregion containing bright extended objects as well as small faint sources. The sky-subtracted images in the third column emphasize that galaxy light sacrificed by the standard OOPS algorithm is retained with median filtering.

To quantify how much light was gained with the revised sky subtraction procedure, we measured the fluxes of sources in the

sky-subtracted images using the methodology of Chies-Santos et al. (2015). Fluxes of galaxies in the right-hand panel of Fig. 5(b) are higher by a median of ∼37 per cent versus the OOPS image in Fig. 5(a). This boost in flux is not strongly sensitive to either dr or the total filter size drdθ. We repeated this test for filters with dr values of 1–5 pixels (at fixed drdθ of 170 pixel radians), as well as for drdθ values of 10–30° at $r = 2$ arcmin (with d$r = 3$ pixels). The resulting median flux ratios deviate by ∼1–3 per cent from the ∼37 per cent value obtained with the adopted fiducial filter parameters (d$r = 3$ pixels, drd$\theta = 170$ pixel radians).

This filtering technique is implemented in PYTHON using standard libraries, including `Astropy` (Astropy Collaboration et al. 2013). We are assisting with the incorporation of this technique into OOPS so that all users of OSIRIS will have access (Ederoclite, private communication).

5 SUMMARY

In this Letter, we have used data from the red TF mode on OSIRIS to demonstrate new techniques for wavelength calibration and sky subtraction. Central to our methodology is the use of polar coordinates, which simplifies matters when the TF data is circularly symmetric. In Section 3, we outlined a technique for wavelength recalibration using OH sky emission rings. This approach increases the accuracy of the absolute wavelength calibration from ∼5 to 1 Å, or ∼7 per cent of the instrumental resolution. In Section 4, we presented a new method to estimate the sky background by median filtering in polar coordinates. The merit of this approach is that of light from the extended haloes of emission-line galaxies does not contaminate the background sky maps. Sources in the associated sky-subtracted images will likely be significantly brighter than how they would appear in images based on the current sky subtraction algorithm in the OOPS. Future OSIRIS/OOPS users will be benefitted from this sky subtraction method.

ACKNOWLEDGEMENTS

This Letter is based on observations made with the GTC, installed in the Observatorio del Roque de los Muchachos of the Instituto de Astrofísica de Canarias, on the island of La Palma. The GTC reference for this programme is GTC2002-12ESO. Access to GTC was obtained through ESO Large Programme 188.A-2002.

REFERENCES

Astropy Collaboration, Robitaille T. P. et al., 2013, A&A, 558, A33
Bland-Hawthorn J., Jones D. H., 1998, PASA, 15, 44
Chies-Santos A. et al., 2015, MNRAS, 450, 4458
Cepa J., 2013, Rev. Mex. Astron. Astrofis. Ser. Conf., 42, 77
Cepa J. et al., 2013, in Diego J. M., Goicoechea L., Gonzãlez-Serrano J. I., Gorgas J., eds, Astrophysics and Space Science Proceedings, Highlights of Spanish Astrophysics V. Springer-Verlag, Berlin, p. 15
Ederoclite A., 2012, The OSIRIS Offline Pipeline Software (OOPS), available at: http://www.aeiou-institute.org/home/technology/software-for-astronomy/oops
González J. J., Cepa J., González-Serrano J. I., Sánchez-Portal M., 2014, MNRAS, 443, 3289
Gray M. E. et al., 2009, MNRAS, 393, 1275
Hanuschik R. W., 2003, A&A, 407, 1157
Osterbrock D. E., Fulbright J. P., Martel A. R., Keane M. J., Trager S. C., Basri G., 1996, PASP, 108, 277

This paper has been typeset from a TEX/LATEX file prepared by the author.